

Geophysical interpretation for delineating groundwater and subsurface structure in the East of Cairo City, Egypt

Esraa Azmy^{1,*}, Sultan Araffa², Ahmed Helaly¹

¹ Ain Shams University, Department of Geophysics, 11566 Cairo, Egypt.

² National Research Institute of Astronomy and Geophysics, 11722, Helwan, Cairo, Egypt.

*Corresponding Author: esraazmy@yahoo.com

ARTICLE INFO

Article History:

Received: June 26, 2021

Accepted: June 30, 2021

Online: July 19, 2021

Keywords:

3D Modeing

RTP

Euler Deconvolution

Groundwater

Rose diagram.

ABSTRACT

This study aimed to delineate groundwater and the structural trends in the East of Cairo City. For this aim, we carried out different geophysical approaches such as gravity, magnetic, and electric methods. For the gravity and magnetic data analysis, we used filtering, Euler deconvolution, and radially power spectrum techniques. In addition, 3-D modeling was performed on the magnetic data only. The radially power spectrum technique shows that the depths of the surface anomalies corresponding to the short wavelength are 0.48 and 0.5 km. While, the depths of the surface anomalies corresponding to the long wavelength are ranging from 2.74 to 2.33 km from gravity and magnetic interpretation, respectively. The Euler deconvolution revealed that investigation area was under the effect of several fault trends; a major NW-SE trend and NE-SW and NW-SE as minor trends for gravity data. While the fault trends are in N-S and NE-SW directions for RTP magnetic data. The 3-D modeling results show that the basement depth was fluctuating between 1.186 to 1.657 Km. The principal tectonic deformations of the investigating area are towards the E-W, N-S, and NE-SW trends. The gravity and magnetic techniques in this study revealed that different faults dissect the area of trends NE-SW matching the Gulf of Aqaba direction, NW-SE matching the Gulf of Suez, N-S matching the River Nile system, and E-W matching the Mediterranean tectonics. The geo-electrical method was used to investigate groundwater presence. Regarding the seismicity, the area can be considered moderate to highly active. Most of the area faults are active except in the area southern part. So, this part can be considered the most suitable and safe part for constructions.

INTRODUCTION

Urban planning comprises many aspects; an important aspect among these ones is to study the geology of the target area. Integrated potential geophysical investigations detect the thickness of sedimentary coverage, depth to the basement relief and subsurface structures structures (Araffa *et al.*, 2017; Araffa *et al.*, 2019; Mohamed *et al.*, 2019; Geng *et al.*, 2020).

The structural trends delineation and the subsurface basement depth involve the gravity and magnetic data integration. This integration is accomplished by applying several

geophysical techniques to get an improved understanding of the target area geology. Gravity and magnetic methods give an efficient demonstration of the subsurface structures.

In gravity prospecting, lateral variations within earth's internal structure are the most important concern, because they indicate density lateral variations (**Foulger and Pierce, 2007**). The gravity method depends on the different earth materials with different bulk densities, causing differences in the measured gravitational field. These differences can be interpreted through several analytical and computational methods to define the geometry, depth and density of subsurface causative features (**Mickus, 1980**).

The nature of the magnetic anomaly of a given magnetized body is more complicated than the gravity anomaly of the same body boundaries (**Luo *et al.*, 2010**). This is because the gravity anomaly depends only on the density contrast and the geometry of the body. But, in the case of the magnetic method, many factors affect the distribution of surface anomalies such as the direction of the magnetic field of the earth and its strength, magnetic susceptibility of the feature causing anomalies, the body orientation with regard to the magnetic field of the earth, and the direction of observation concerning body axes.

The geo-electrical method was used to explore groundwater. The electrical resistivity technique was applied to investigate the saturated zone with groundwater. The investigation area covers about 1250 Km². It is located to the Eastern side of Cairo governorate; between latitudes 30° 05' N & 30° 30' N, and longitudes 31° 25' E & 31° 40' E (Figs.1a, b). the area is bounded by Sharqia Governorate from the North, the Cairo-Suez road from the South, 10th of Ramadan & Badr cities from the East and the Damietta branch from the West. This area includes new urban cities as 10th of Ramadan, New Al-Obour, and Badr cities.

Many studies were done near and around the area (**Sultan *et al.*, 2011; Araffa, 2013; Araffa *et al.*, 2014**). The current study targets to provide a complete image about the structures of subsurface and relief of basement rocks of the investigation area. Likewise, recognize the occurrence of groundwater in the investigation area.

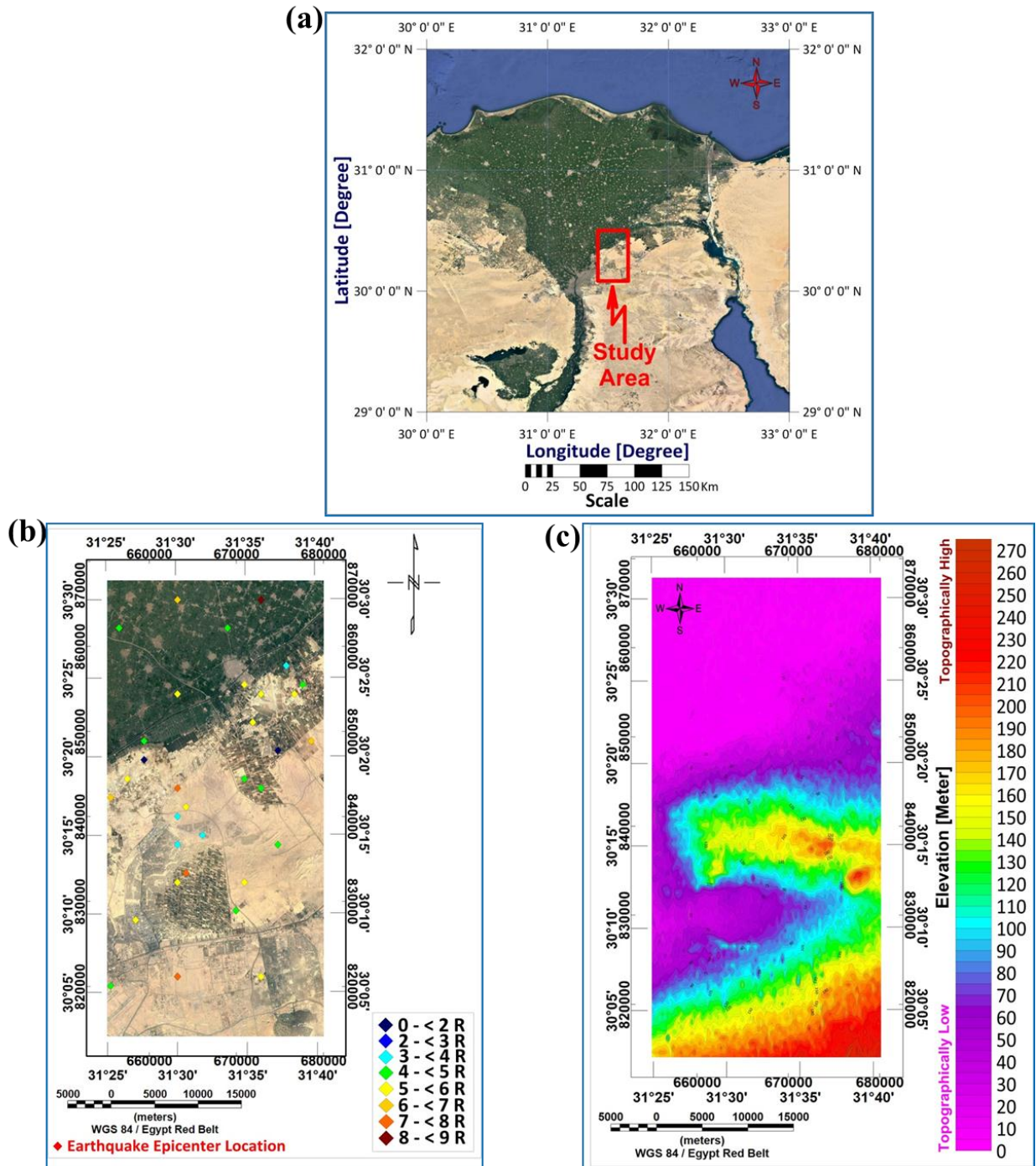


Fig. 1. (a) Area Location; (b) Satellite image, and c Area Surface topography using digital elevation model (DEM).

GEOLOGIC SETTINGS

The study area has a relatively low relief on the northern part, while the middle and the southern parts include more rugged relief. The area elevations are ranged between 0 m at the West, and 270 m at the G. El Hamza at the East (Fig. 1b). Like the whole Cairo-Suez district, the target area includes geomorphic landforms reflecting

semiarid climate. There are five differentiated landforms; each landform consists of a set of local units. Lithologically, these units are composed of Quaternary sands & gravels and are common in the southern portion of the area. The low relief area comprises three geomorphic landforms; rolling plains, sand dunes, and dried wadies. In contrast, the rugged area comprises two other geomorphic landforms; structural high-table lands and flat-topped hills.

Regarding the stratigraphy (Fig. 2), the sedimentary rocks belong to the Quaternary and Tertiary rock units. The Quaternary sediments are divided into Holocene and Pleistocene sediments. Holocene is characterized by variable unconsolidated sediments like young wadi fill deposits and young Aeolian deposits (**El-Fayoumy, 1968**). The Pleistocene deposits comprise the old deltaic deposits that consist of flinty pebbles of igneous fragments and coarse sand. Tertiary rock units composed of Pliocene marl dolomite and sandy limestone in Cairo northeastern side. Miocene rock units have a widespread distribution in the southern high slopes, formed sandy marls and sandy limestone. Oligocene rocks units are composed of sands, gravels and volcanic basalts. Eocene fossiliferous beds (chalky, marly, dolomitic, and sandy limestone) belong to Middle and Upper Eocene (**Mohamed and El-Sabrouy, 2014**).

Structurally, the investigation area is affected by normal dip-slip faults; the majority of these faults are oriented towards the E-W and N-W directions. The existing en-echelon folds are asymmetric and doubly plunging, they are represented by two alternative anticlines and synclines. These folds are oriented in ENE to NE direction. There is an old regional unconformity between the Oligocene and Eocene formations just south of the study area. In addition, there are five local unconformities arranged from older to younger (**Hashem, 1997**) as follows:

- 1- The Oligocene sands and gravels - Basaltic flows unconformity; this surface is well represented in several localities to the western foot slope of G. El-Hamza anticline flank.
- 2- The basaltic flow-Lower Miocene unconformity.
- 3- The Lower Miocene-Middle Miocene unconformity.
- 4- The Middle Miocene - Upper Miocene unconformity.
- 5- The Upper Miocene - Quaternary unconformity.

This study aims to give an informative picture of the faults, groundwater occurrence, and definition of the basement relief in the area that located at the East of Cairo City and is targeted to be an urban area. The fault traces delineation helps to decide the suitability of the area for new cities establishment through an integrated geophysical study.

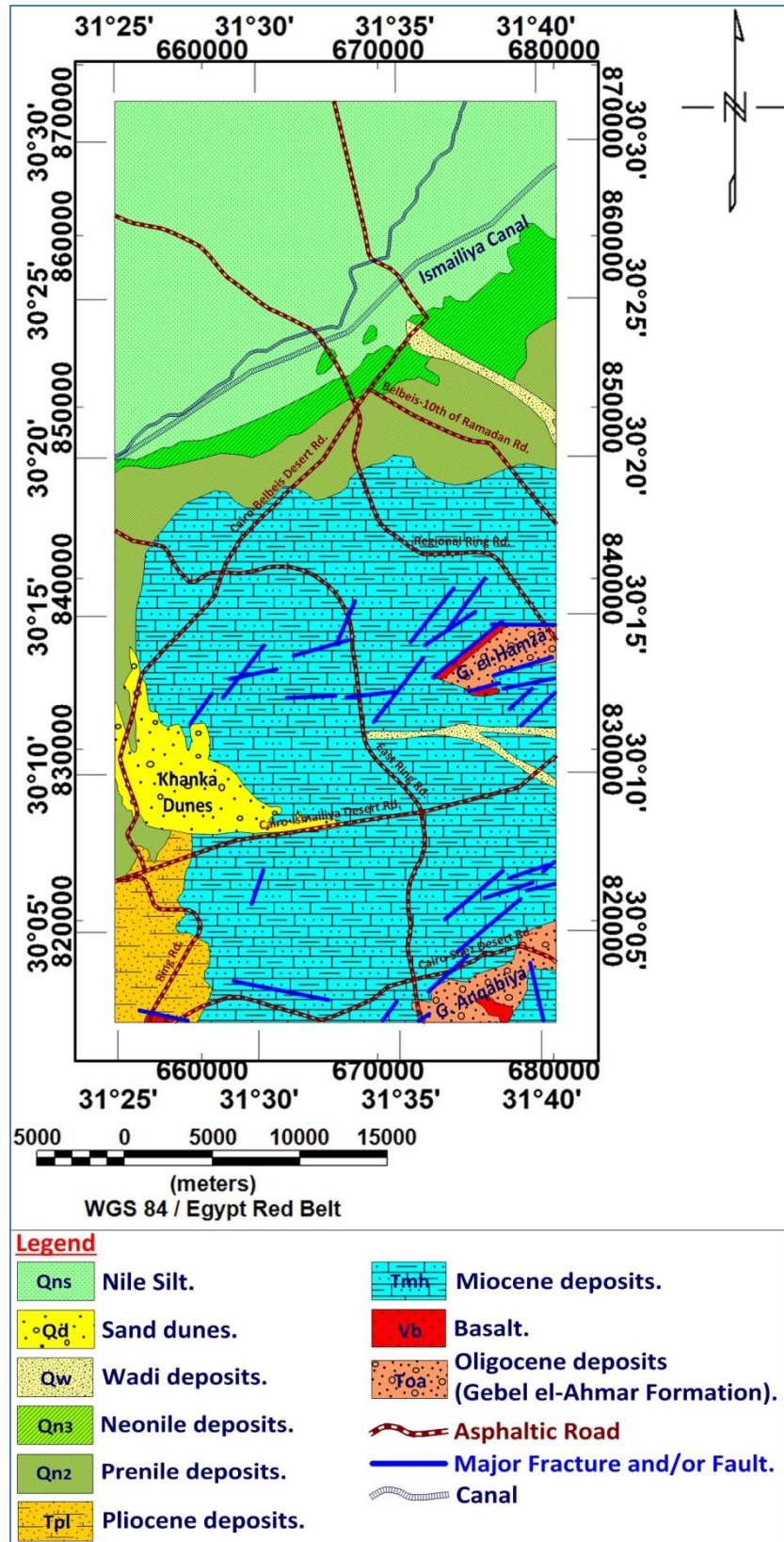


Fig. 2. Area geological map (after CONCO, 1987).

METHODS

The gravity, magnetic, and electric methods and the seismicity were applied to delineate the structural trends, groundwater, and the subsurface basement depth of the area, and to detect the parts that can be considered the most suitable and safe ones for constructions.

Gravity Method

The gravity data were collected by EGSMA (Egyptian Geological Survey and Mining Authority) in the period from 1994-1997. The gravity field measurements were completed with the automated Gravity-meter (CG-3 Autograv, Scintrex Company, Canada, 1992). The survey design was divided into a regular grid of 500 x500 m with total numbers of stations. Different data corrections were applied to gravity data such as elevation, drift, latitude, tide corrections, and topography. The corrected gravity data were represented by Bouguer map.

Bouguer Anomaly Map

The Bouguer map (Fig. 3) shows major wide strong positive anomalies (red) in the study area northern half, while there are major wide strong negative anomalies (blue) in the map southern half. The map reveals that the gravitational field rises towards the north direction.

Radially Averaged Power Spectrum Technique

It was executed to determine the basement relief, volcanic intrusions, and subsurface structures. The spectral analysis (Power Spectrum Curve) was performed depending on the gravity data interpretation through Fourier Transform (FFT) (**Spector and Grant, 1970; Garcia and Ness, 1994; Maurizio *et al.*, 1998**).

The FFT was performed on the gravity data to estimate the energy spectrum. The calculated radially-averaged power spectrum (Fig. 4a) revealed that the deep-seated component of gravity frequency (first segment, regional component) changed from 0.0 to 0.11144 cycles/grid unit. In contrast, the near-surface gravity component frequency (second segment, residual component) was ranged from 0.11144 to 0.28212 cycles/grid unit. The line slope of both the 1st and 2nd spectrum curve segments was obtained to calculate the average depths of residual and regional gravity sources. The calculated average depths of the residual and regional sources were 0.48 km and 2.74 km, respectively.

Regional-Residual Separation

Wavelength filtering is based on the wavelength which is correlated to the body depth; the filtering techniques separate anomalies of diverse wavelengths (**Foulger and Pierce, 2007**). The regional deep anomalies have low frequencies or long wavelengths (regional component), while the local shallow anomalies have high frequencies or short wavelengths (residual component). The 2-D filtering technique was performed on the Bouguer map by using the low and high pass filters with the efficient cutoff wavelengths.

The previously gridded and contoured Bouguer map was separated into its residual and regional components via Oasis Montaj (v.8.4, 2015).

The high pass filtration was performed on the Bouguer map with a 0.09559206 cycle/ unit wavelength. The high-pass map (Fig. 4b) displayed several positive (red) and negative (blue and green) anomalies. Some anomalies were elongated, and the others were semicircular in shape. The anomalies were in the directions E-W, N-S, NE-SW, and NW-SE. The residual gravity anomalies can be interpreted regarding the structural elements and lithologic variations in the shallow range depth. The lithologic inferences can be limited to the sedimentary section thickness and the basaltic sheet intrusion in the shallow part of the sedimentary section.

The low pass filter was applied to the Bouguer map with wavelength of 0.09559206 cycle/ unit. The low-pass or regional filtered map (Fig. 4c) showed a rise in the positive gravity anomalies (red), which are found in the middle of the map. These anomalies are in the directions N-S, NW-SE, and NE-SW.

The negative anomalies (blue) occupied the southern portion of the map, with E-W, and NE-SW directions.

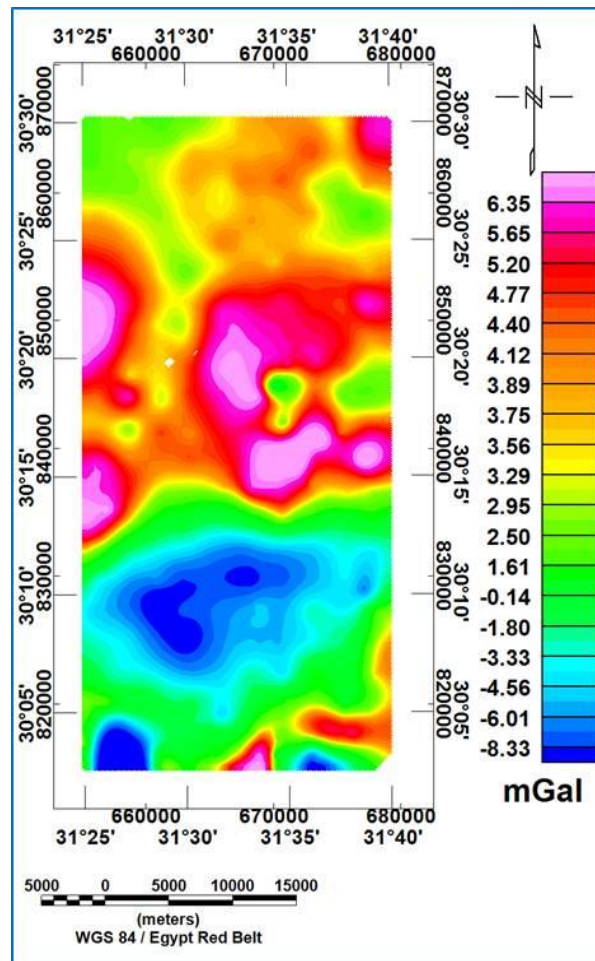


Fig. 3. Bouguer map of the survey site.

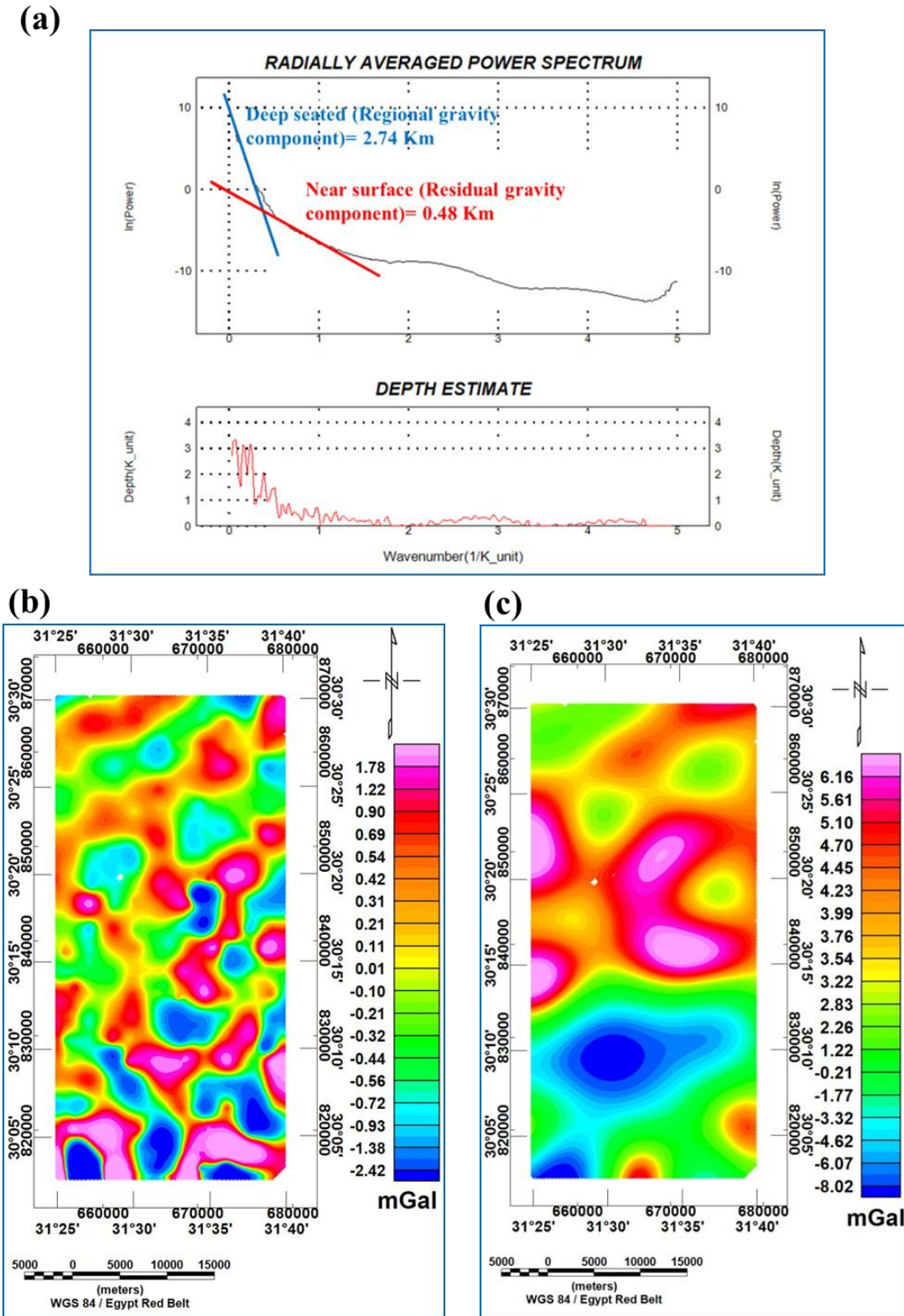


Fig. 4. (a) 2-D radially averaged power spectrum; (b) Residual; and (c) Regional map.

Euler Deconvolution

This technique is considered as an interpretation method to locate anomalous sources and determine their depths (Thompson, 1982; Afolabi *et al.*, 2012).

The equation of homogeneity is written as the following according to Reid *et al.*, (1990):

$$(x - x_0) \frac{\partial T}{\partial x} + (y - y_0) \frac{\partial T}{\partial y} + (z - z_0) \frac{\partial T}{\partial z} = N(B - T).$$

As (x_0, y_0, z_0) is the magnetic source location with (T) total field detected on (x, y, z) ,

(B) background value, (N) the falloff rate of the magnetic field, it can be considered as the (SI) structural index depths (Thompson, 1982). This technique can be used for the depth estimation of extensive geological features like contacts, faults, and dykes. It is suitable for anomalies formed by multiple and isolated sources (El Dawi, 2004; El-Awady, 2016). The depth estimation is dependent on choosing of suitable data sampling and structural index (SI) . Euler Deconvolution was performed on the Bouguer data via the Oasis Montaj (v.8.4, 2015) at different levels of calculations with structural indices; $SI=0$, $SI=0.5$, $SI=1$, and $SI=2$ (Fig. 5).

Gravity Data Analysis and Interpretation

The results of the high and low pass filtering technique were used to determine the fault system distribution that probably exists in the investigation area surface and subsurface. The high pass filtering technique clarified the residual sources which represent the shallow-seated subsurface features. The fault trends in the high pass filtered map were displayed in the rose diagram using GeoRose program (Figs. 6a, b). The major fault trends were found to be N-S and NE-SW directions.

The low pass filtering technique deduced the regional sources which represent the deeper-seated depths. The fault trends in the low pass filtered map were displayed in the rose diagram (Figs. 6c, d). The major fault trends were in directions NE-SW and E-W. After applying the Euler deconvolution to the Bouguer map, it was found that the best chosen structural index was $SI=0$. The fault trends in the Euler solution map were displayed in rose diagram (Fig. 7). The circles of the linear clustering are assumed to be resulted from fault trends. These resulted solutions are directed in NW-SE as a major trend and NE-SW, NW-SE as minor trends.

The results of the high, low pass filtered and Euler solution maps indicated the coincidence of the fault trends with the directions of the Gulf of Suez, Gulf of Aqaba, River Nile system, and Mediterranean tectonics. The rose diagrams (Fig. 8) displayed the tectonics orientation deduced from the low, high filtered, and Euler solution maps. Through the inspection of the rose diagrams, it can be noticed that the most common tectonic trends prevailing in the deeper levels are the NE-SW (45° - 60°) and E-W. On the other hand, the most common tectonic trends prevailing in the shallow levels are N-S and NE-SW (45° - 60°). While the dominant tectonic trend from the Euler solution is $N45^\circ W$ prevailing in shallow-intermediate levels.

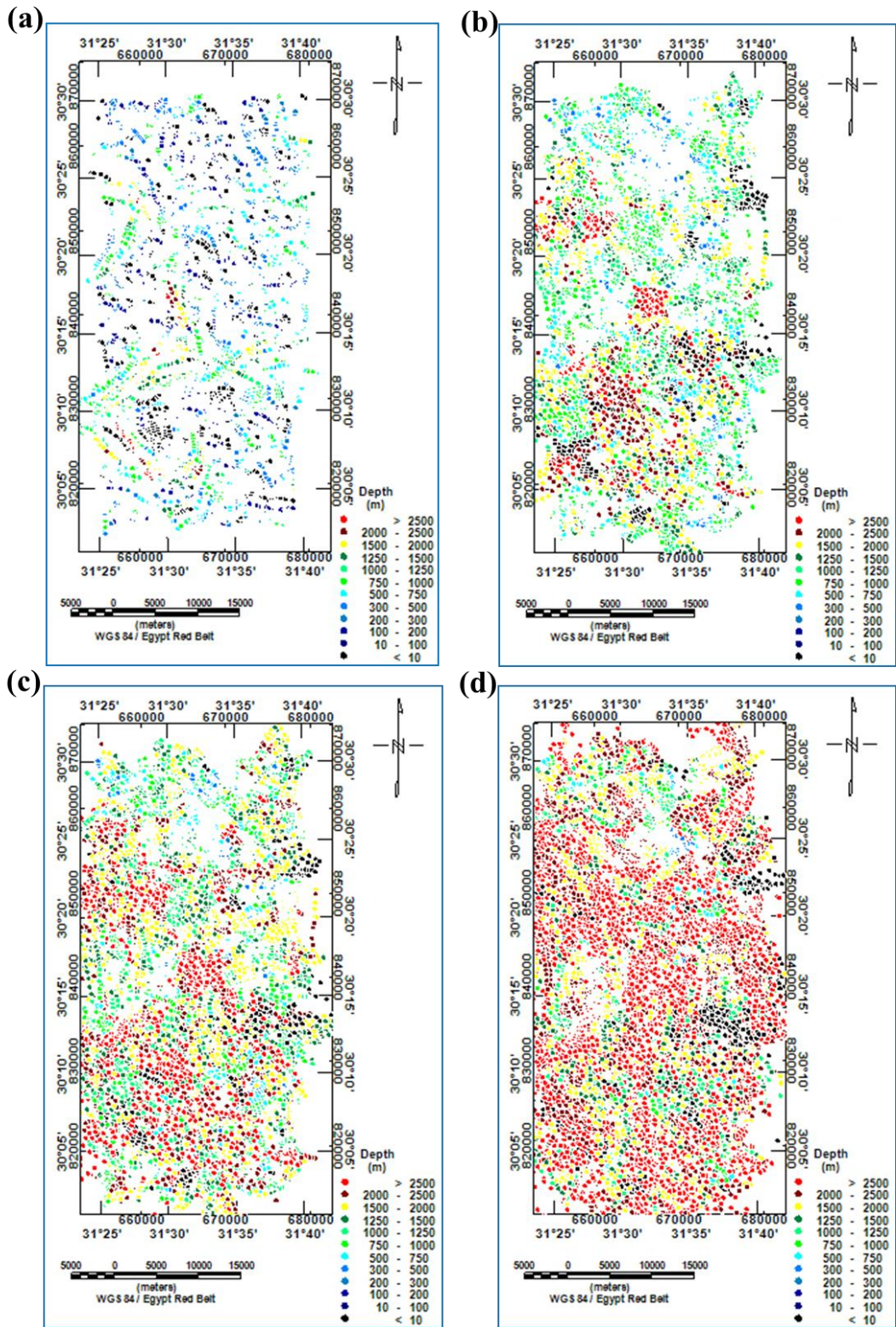


Fig. 5. (a) Euler solution plot via structural index S.I. = (0); (b) Euler solution plot via S.I. = (0.5); (c) Euler solution plot via S.I. = (1); and (d) Euler solution plot via S.I. = (2) of gravity data.

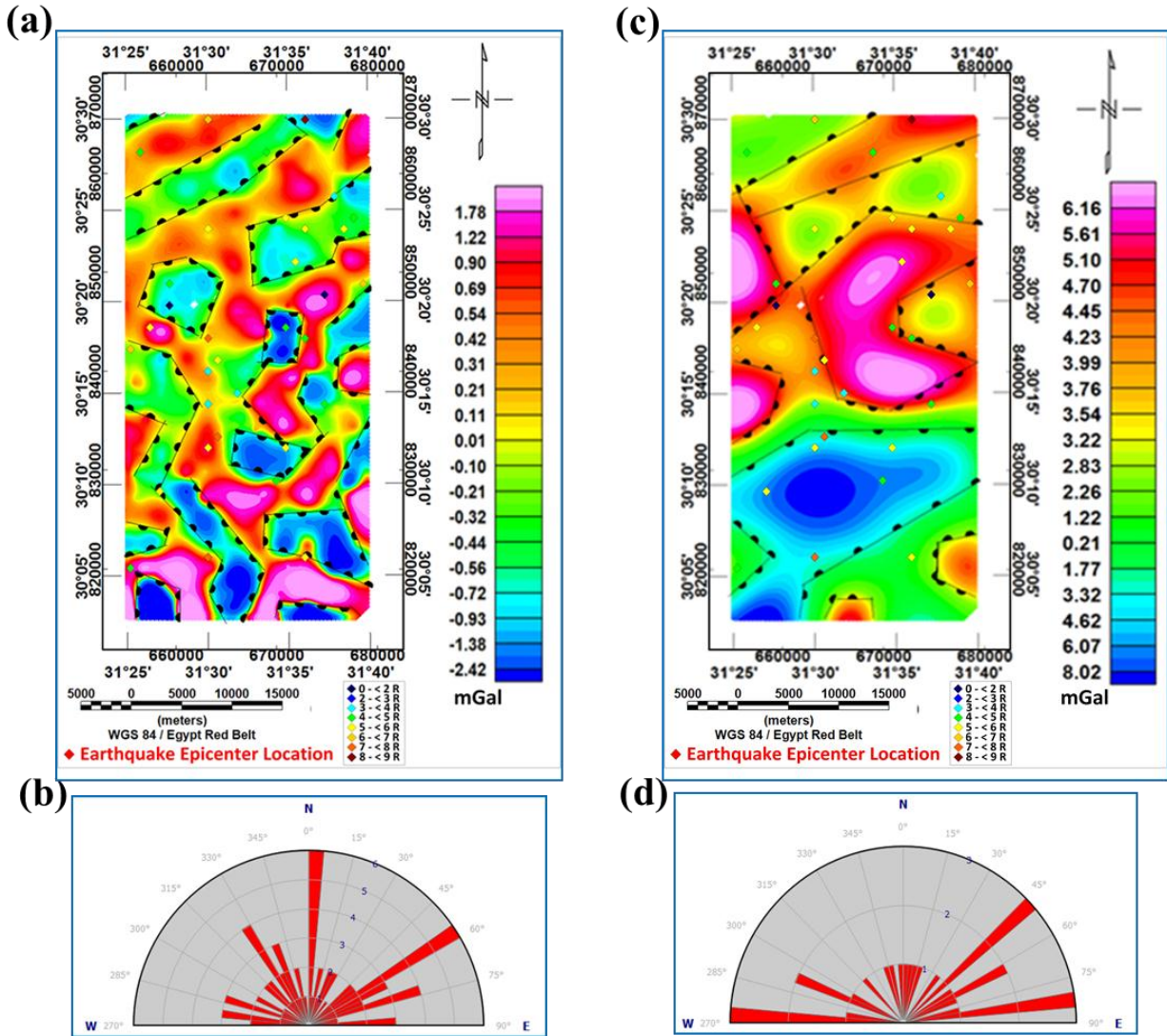


Fig. 6. (a) Fault trends deduced from residual gravity filtered map and earthquake epicenter locations; (b) Rose diagram assumed from high pass gravity filtered map; (c) The fault trends deduced from regional gravity filtered map and earthquake epicenter locations; and (d) Rose diagram assumed from low pass gravity filtered map.

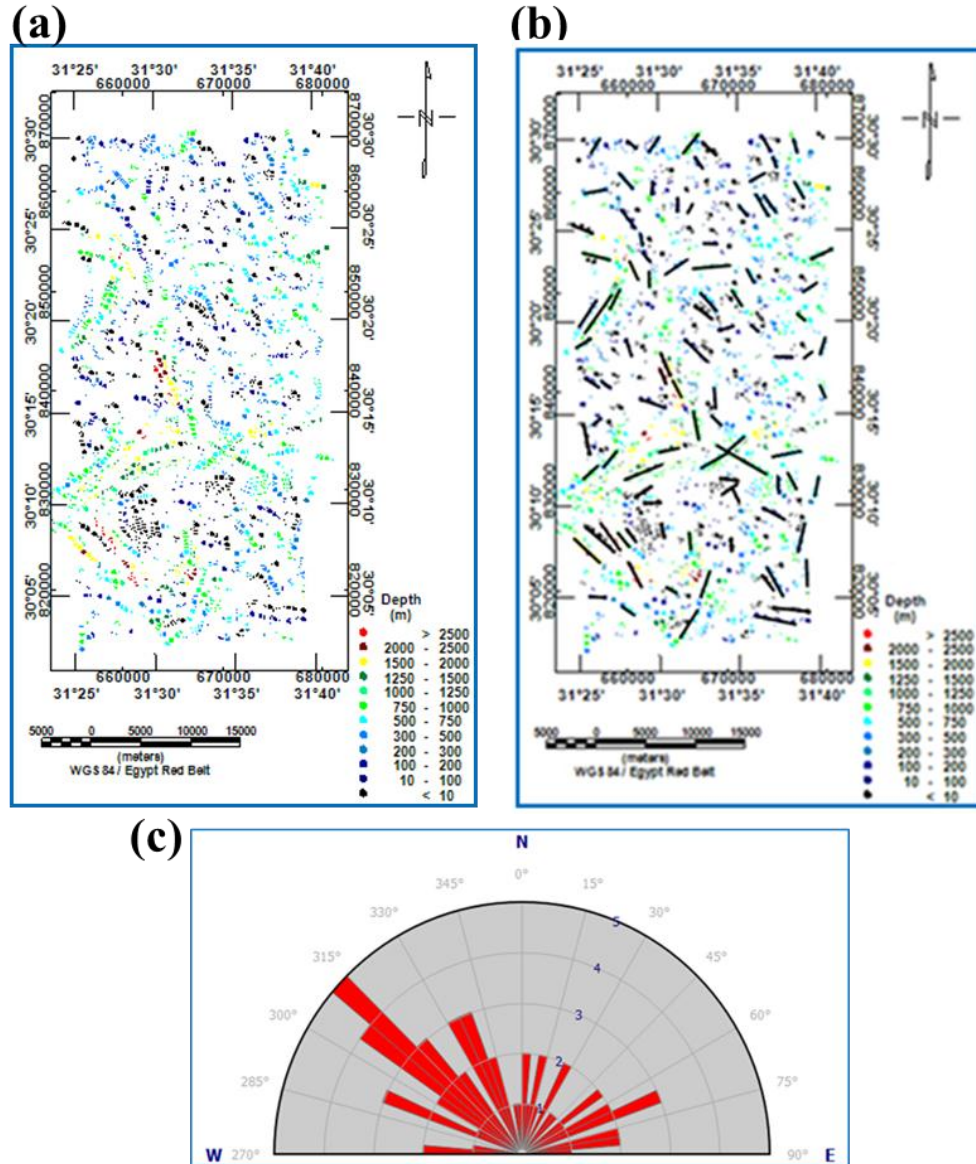


Fig. 7. (a) Map of Euler solution plot of gravity data via structural index $S.I. = 1$; (b) Map showing the fault trends of gravity data, and c Rose diagram deduced from Euler solution.

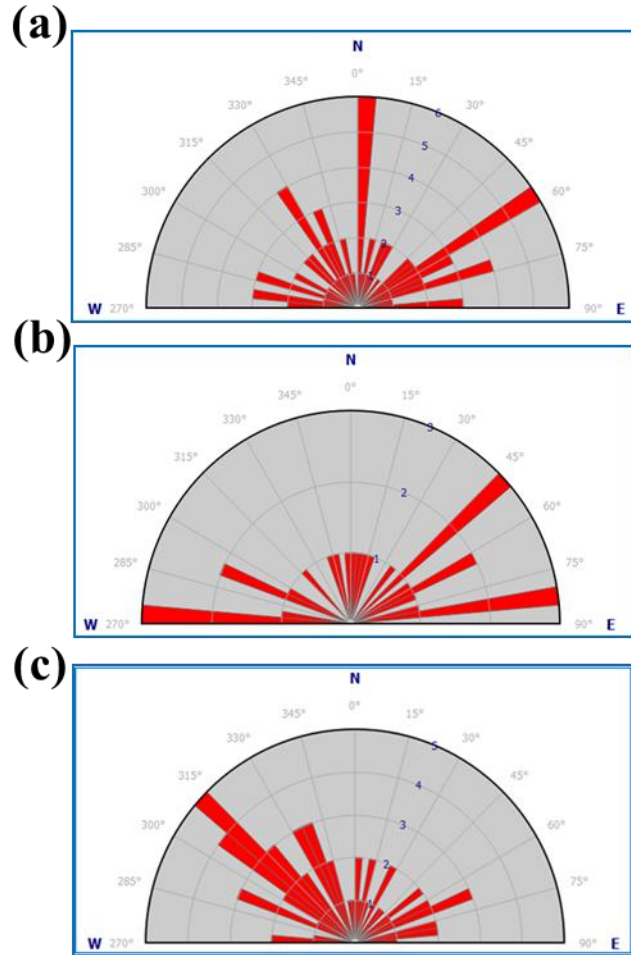


Fig. 8. Rose diagrams deduced from (a) High pass; (b) Low pass gravity filtered map; and (c) Euler solution using $SI=0$.

Magnetic Method

The magnetic data were collected from EGSM through the period from 1994-1997 and the survey design was divided into a regular grid of 500 x 500 m with total numbers of stations. The magnetic data were measured using two instruments of ENVIMAG magnetometers (Scintrex Company, Canada, 1992); one was used for collecting the magnetic data and the second was considered to be the base station to calculate the diurnal variation.

Corrections such as diurnal and IGRF were executed to the measured magnetic data, the corrected data was then displayed in the total magnetic intensity map (TMI).

The Reduced to the North Magnetic Pole

The TMI map (Fig. 9a) showed several negative (blue) and positive (red) anomalies. There are two strong positive anomalies in the center and south of the map and many strong negative anomalies in the northern and eastern portions of the map. The TMI map was reduced to the pole through the automatic calculation via Oasis Montaj

(v.8.4, 2015) with input parameters; inclination angle (44.34°), declination angle (3.147°), and magnetic field strength (43319.9 nT).

A general view of the RTP map (Fig. 9b) compared to the original TMI map (Fig. 9a) showed a northward shift in the original anomalies locations. The anomalies were shifted to be directly over their relevant causative sources centers and their sizes increased. The anomalies gradients became more intensive and steeper causing an increase in encountered structural resolution and lithological inferences. It is important to mention that, the positive (red) and negative (blue) magnetic anomalies previously defined in the total intensity magnetic map (Fig. 10a) became more obvious in the RTP map (Fig. 10b). As a result of the mentioned shift, some anomalies appeared in the map northern and southern portions with steep amplitudes. Moreover, some smaller negative and positive anomalies presented in the TMI map became hidden in the RTP map.

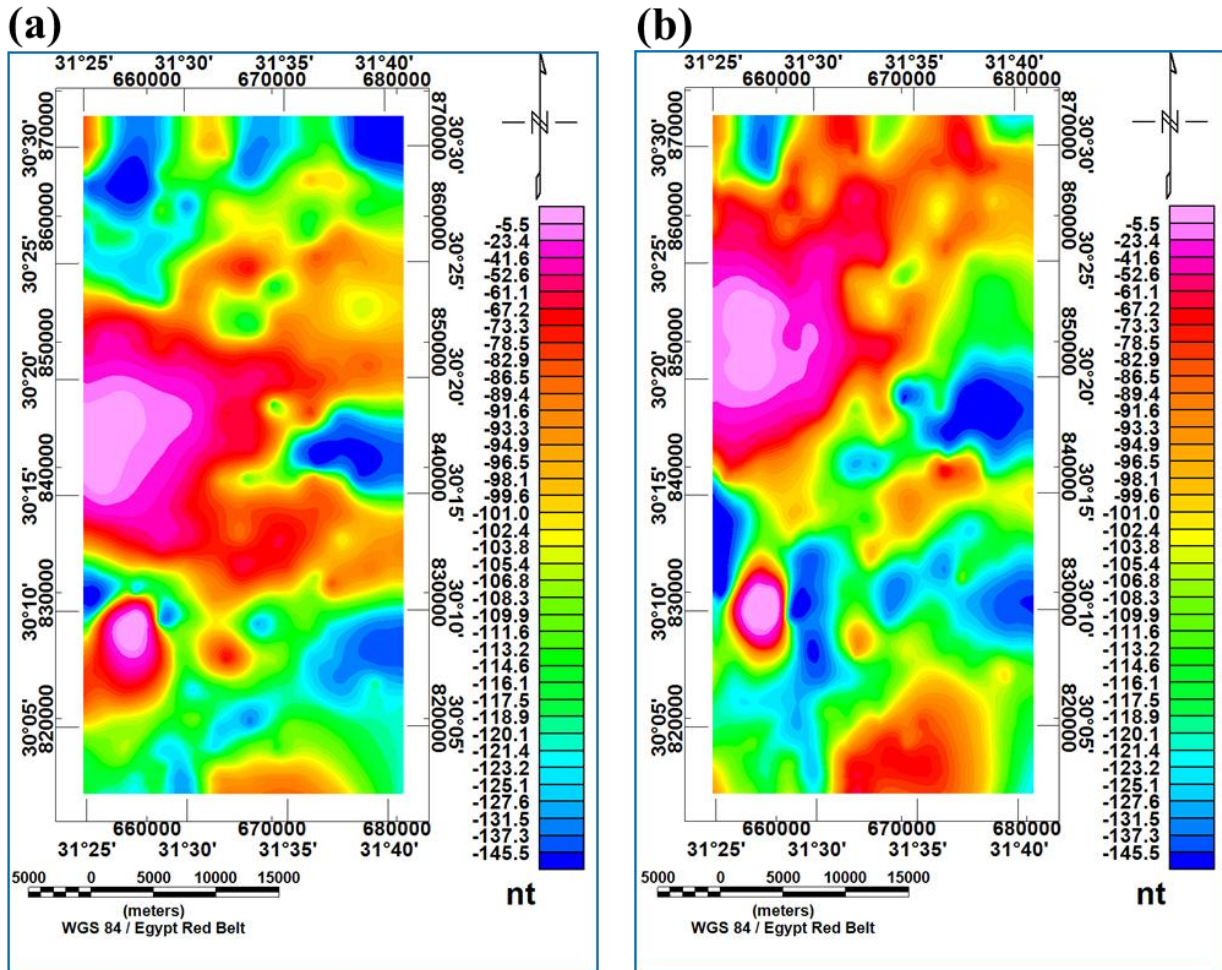


Fig. 9. (a) Total magnetic anomaly; and (b) RTP map.

Radially Averaged Power Spectrum Technique

The FFT was executed to the RTP data. The calculated radially-averaged power spectrum (Fig. 10a) revealed that the deep-seated component frequency (first segment, regional component) changed from 0.0 to 0.1858 cycles/grid unit. In contrast, near-surface component frequency (second segment, residual component) was ranged from 0.1858 to 0.4713 cycles/grid unit. The slope of the line fitted to the two segments of the spectrum curve is applied for calculation of the average of the regional and residual sources depths. The calculated average depths were 0.5 km and 2.33 km for the residual and regional sources, respectively.

Regional-Residual Separation

The 2-D filtering technique was executed to the RTP map using the low and high pass filters with the efficient cutoff wavelengths. The previously-gridded and contoured RTP magnetic map was separated directly into its residual and regional components.

The high pass filter was executed on the RTP map with a 0.29 cycle/ unit wavelength. The high-pass filtered RTP map (Fig. 10b) displayed several positive (red) and negative (green and blue) anomalies. Some anomalies were elongated, while the others were semicircular in shape. The anomalies were in the directions N-S, NE-SW, and NW-SE. The residual RTP magnetic anomalies can be analyzed through the structural elements and lithologic variations in the shallow depth.

The low pass filter was executed on the RTP map of wavelength of 0.29 cycle/ unit. The positive (red) anomalies (Fig. 10c) were found in three parts on the map; the northwestern, southwestern, and southern portions. These anomalies are in NW-SE directions but with various angles. The negative anomalies (blue) occupied the middle and the southern portion of the map, with E-W, and NE-SW directions.

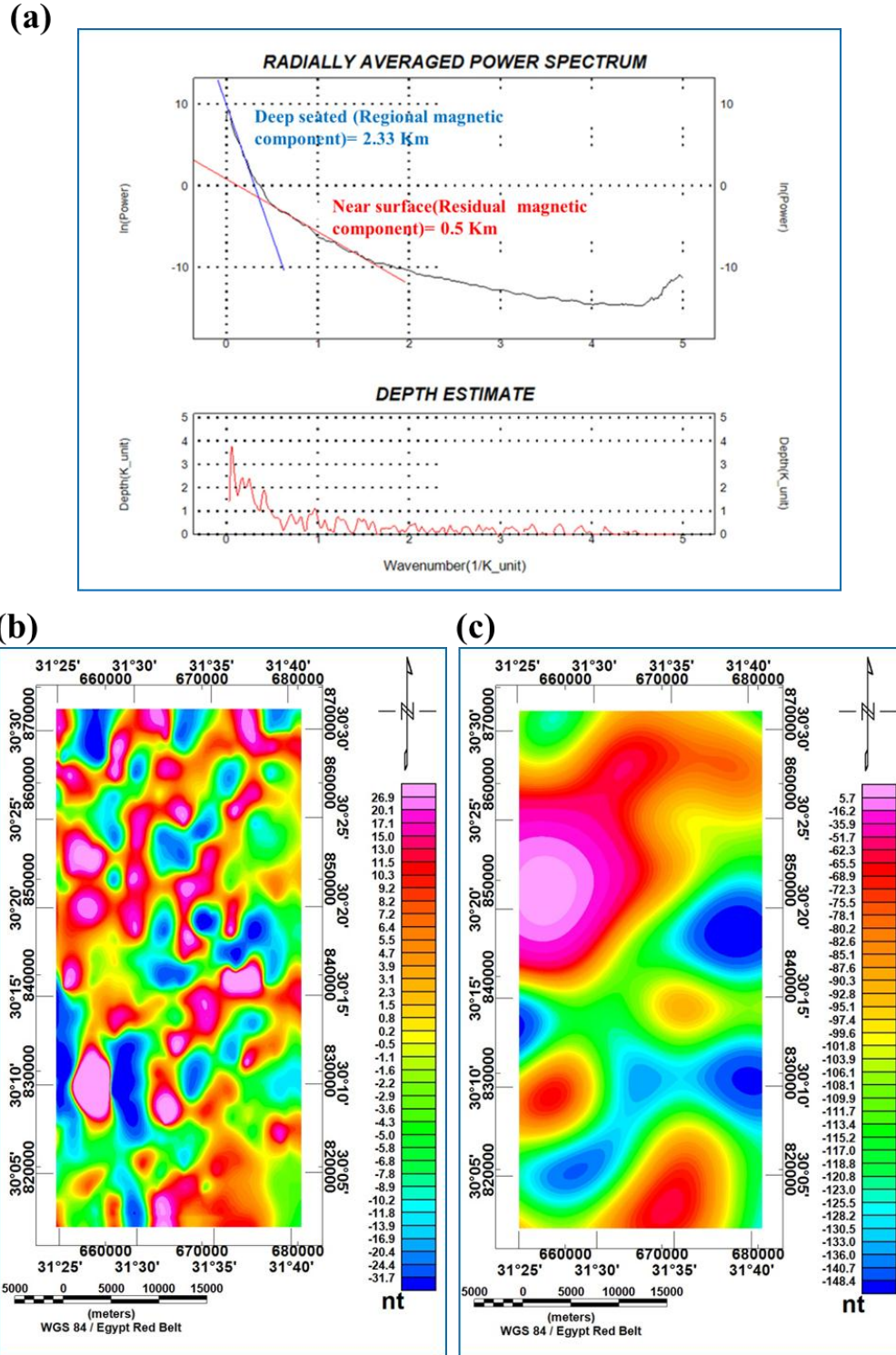


Fig. 10. (a) 2-D radially averaged power spectrum; (b) Residual; and (c) Regional map.

Euler Deconvolution

This technique was performed on the RTP data at different levels of calculations with structural indices; SI=0, SI=0.5, SI=1, and SI=2 (Fig. 11).

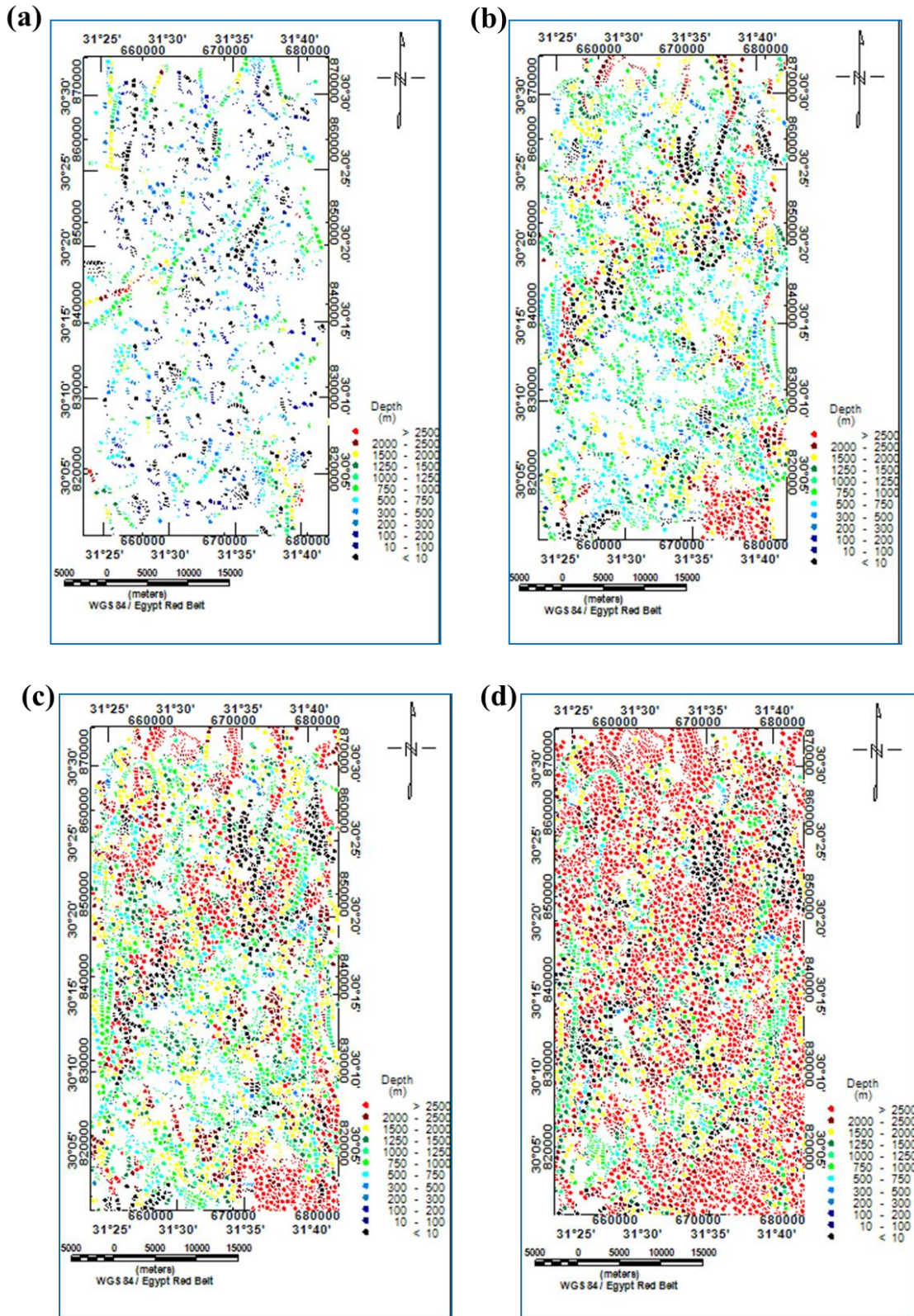


Fig. 11. (a) Euler solution plot via structural index S.I. = (0); (b) Euler solution plot via S.I. = (0.5); (c) Euler solution plot via S.I. = (1); and (d) Euler solution plot via S.I. = (2) of RTP data.

Magnetic Data Analysis and Interpretation

After applying the low and high pass filtering technique on the RTP magnetic map, the results from these techniques were used to determine the fault system distribution that exists in the investigation area surface and subsurface. The high pass filtering technique shed light on the residual sources which represent the shallow-seated subsurface features. The fault trends in the high pass filtered RTP magnetic map were exhibited in the rose diagram (Figs. 12a, b). The major fault trends were found to be NE-SW and N-S.

The low pass filtering technique clarified the regional sources which represent the deeper-seated depths. The fault trends in the low pass filtered RTP magnetic map were displayed in the rose diagram (Figs. 12c, d). The major fault trend was NE-SW.

Using the Euler deconvolution, it was found that the best chosen structural index was $SI=0$. The fault trends in the Euler solution map were displayed in rose diagram (Fig. 13). The fault trends were directed in the directions N-S and NE-SW.

The low, high pass filtered and Euler solution maps results indicated that the most common directions of the fault trends are the same of the gravity data analysis.

The rose diagrams (Fig. 14) revealed the tectonics orientation deduced from the low, high filtered, and Euler solution maps. The most common tectonic trends prevailing in deeper levels are NE-SW tectonic trend (45° - 60°) and E-W tectonic trend. On the other side, the most common tectonic trends in the shallow levels are N-S and NE-SW (45° - 60°). While the dominant tectonic direction from the Euler solution is N-S and NE-SW prevailing in shallow-intermediate levels.

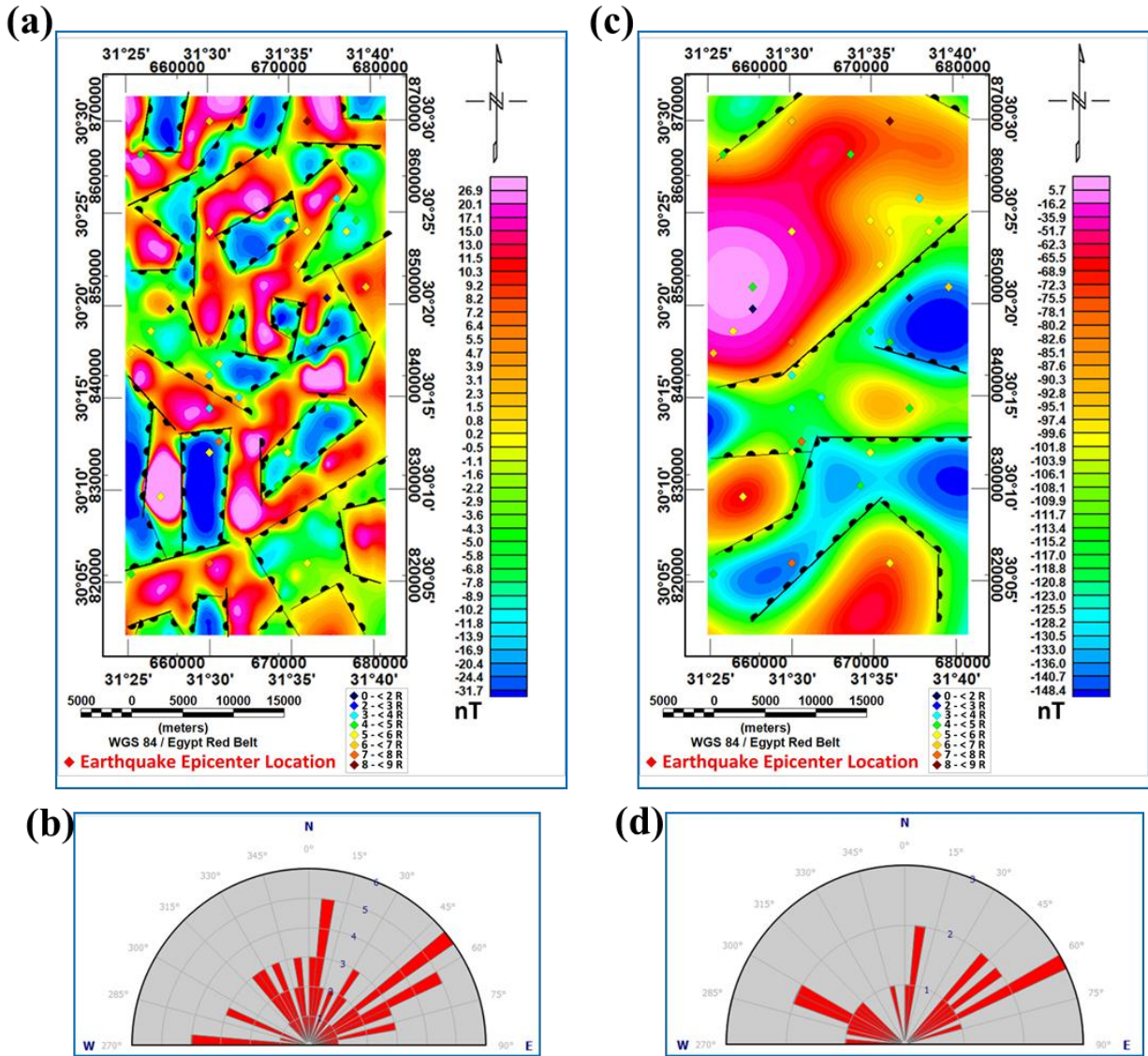


Fig. 12. (a) The fault trends from residual RTP filtered map and earthquake epicenter locations; (b) Rose diagram assumed from high pass RTP filtered map; (c) The fault trends from regional RTP filtered map and earthquake epicenter locations; and (d) Rose diagram assumed from low pass RTP magnetic filtered map.

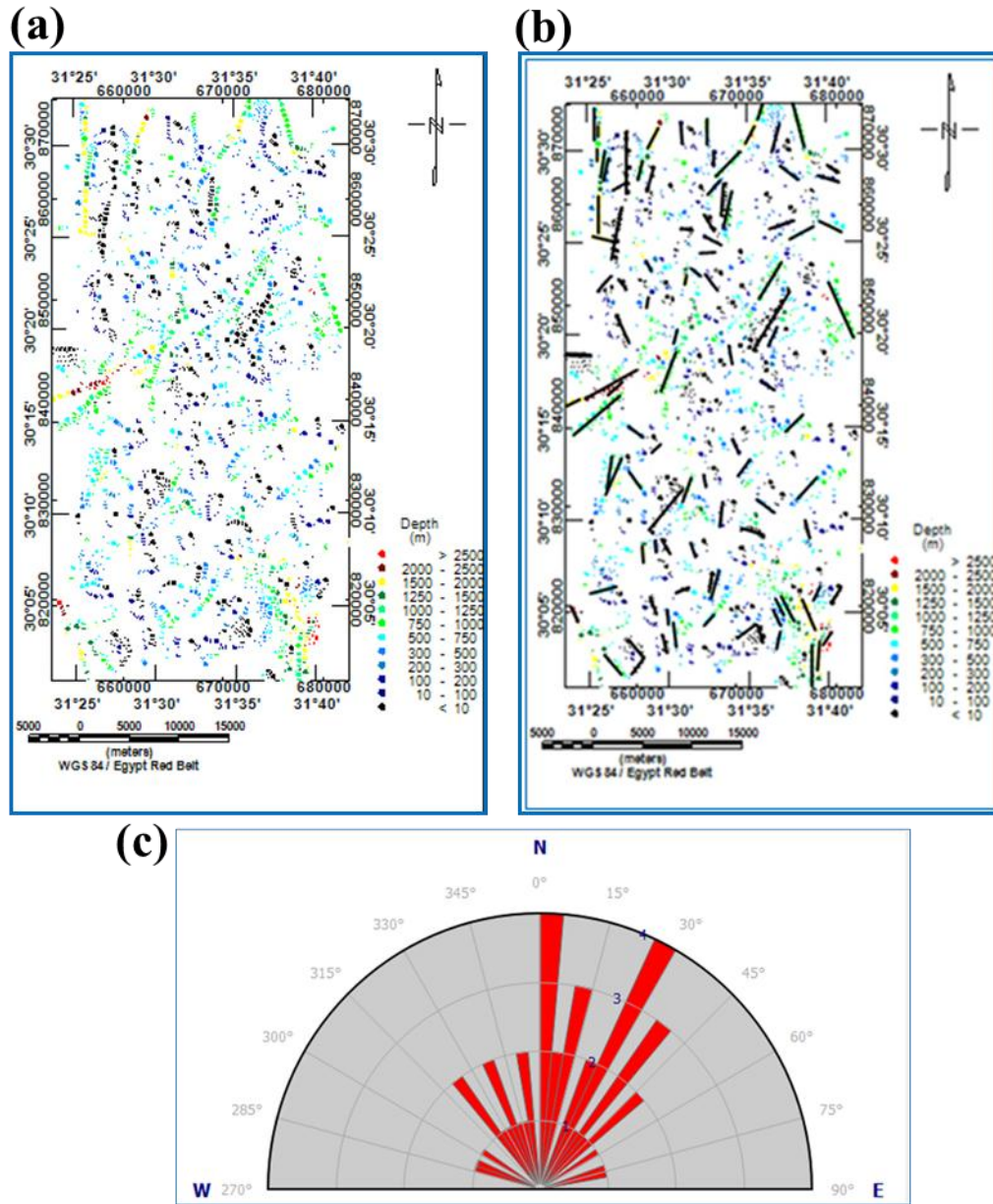


Fig. 13. (a) Map of Euler solution plot of magnetic data via S.I. = 1; (b) The fault trends of magnetic data; and (c) Rose diagram deduced from Euler solution.

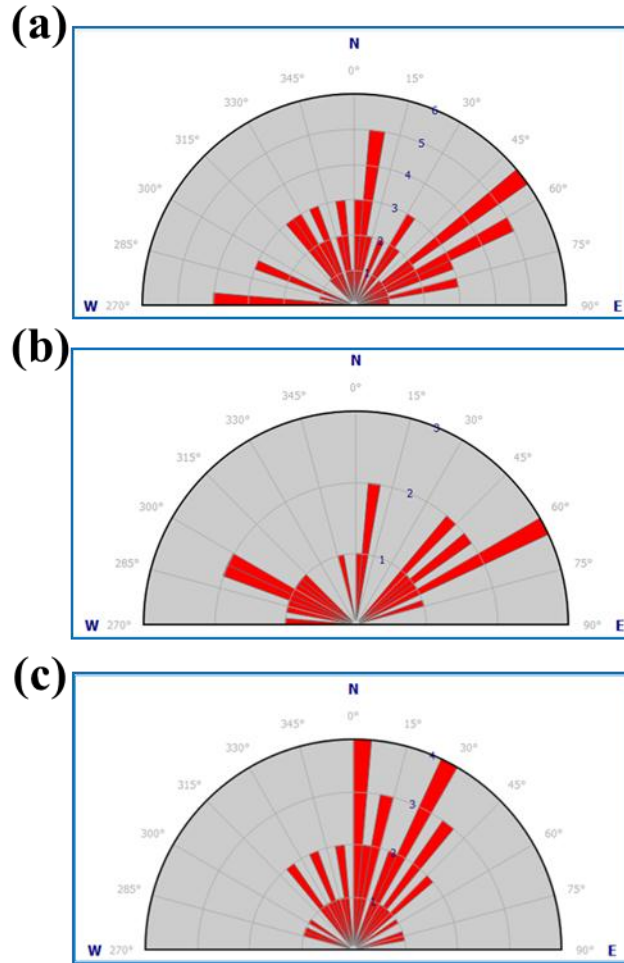


Fig. 14. Rose diagrams (a) High pass; (b) Low pass RTP filtered map; and (c) Euler solution using $SI=0$.

The 3-D Magnetic Modeling

The GM-SYS 3-D (an addition to Oasis Montaj) was executed to detect the top of basement depth and the 3-D model of the subsurface structures.

The 3-D model was built using the observed RTP data; it is supposed that all grids must have the same cell size, dimensions, distance units, and projection. The numbers of the cells used in the X-direction were 255 and in the Y-direction were 540 cells with grid cell size 100 m. The subsurface was divided into two layers; the first represented in the sedimentary section with magnetic susceptibility of 0.0 cgs units and the second represented the basement with magnetic susceptibility approximately equals to 0.00075 cgs units. These values of magnetic susceptibility were referenced by (Araffa *et al.*, 2015).

In addition, the 3-D modeling requires the magnetic field strength values, field declination, and inclination angles. The used values were 43319.9γ , 44.34° , and 3.147° , respectively. It is important to note that, the 3-D modeling is dependent upon two types of the data; the 1st is the fixed observed gridded one, which is represented by the RTP

magnetic data (Fig.15a) and the second is the variable calculated data (Fig. 15b). The fitting between the calculated and observed data was done at the lowest value of error percentage (Fig. 15c). The two principle portions of the final 3-D modeling are the surface topography (Fig.1c) and basement rocks' surface depth (Fig. 15d).

1- The Topographic Surface

The topographic surface values varied from 7.9 m in the northern portion to 290 m forming high topographic features in the investigation area southern part (Fig.1c).

2-The basement rocks depth (upper crust)

Through the interpretation of basement depth map (Fig. 15d); it was observed that the shallow basement surface depth is found in the map northwestern and southern portions and equivalent to 1.186 km beneath sea level. The deeper basement surface is located around the map central region with an approximate depth of about 1.657 km. From the depth to basement results, it can be concluded that the sedimentary cover thickness is about 1.186 km in the northwestern and southern parts and 1.657 Km in the center.

Geo-Electrical Method

The current field measurements were acquired by ABME Terrameter SAS 300 resistivity meter along four vertical electrical soundings via Schlumberger array (Fig.16). The maximum AB/2 got to 900m apart.

Geo-Electrical Data Analysis and Interpretation

The data were interpreted via Moscow State University IPI2win V3.1.2 resistivity sounding interpretation and Golden Surfer 16 softwares. The measured data were imported in the IPI2win software. Log –log graph for the AB/2 spacing against its apparent resistivity values. This graph revealed the observed apparent resistivity curve for each VES. Forward modeling inversion for the data were conducted to acquire the best fit between the measured and calculated apparent resistivity data using an initial model from the geological outcrops and previous geological information at the study area to compute the true resistivity values and thicknesses.

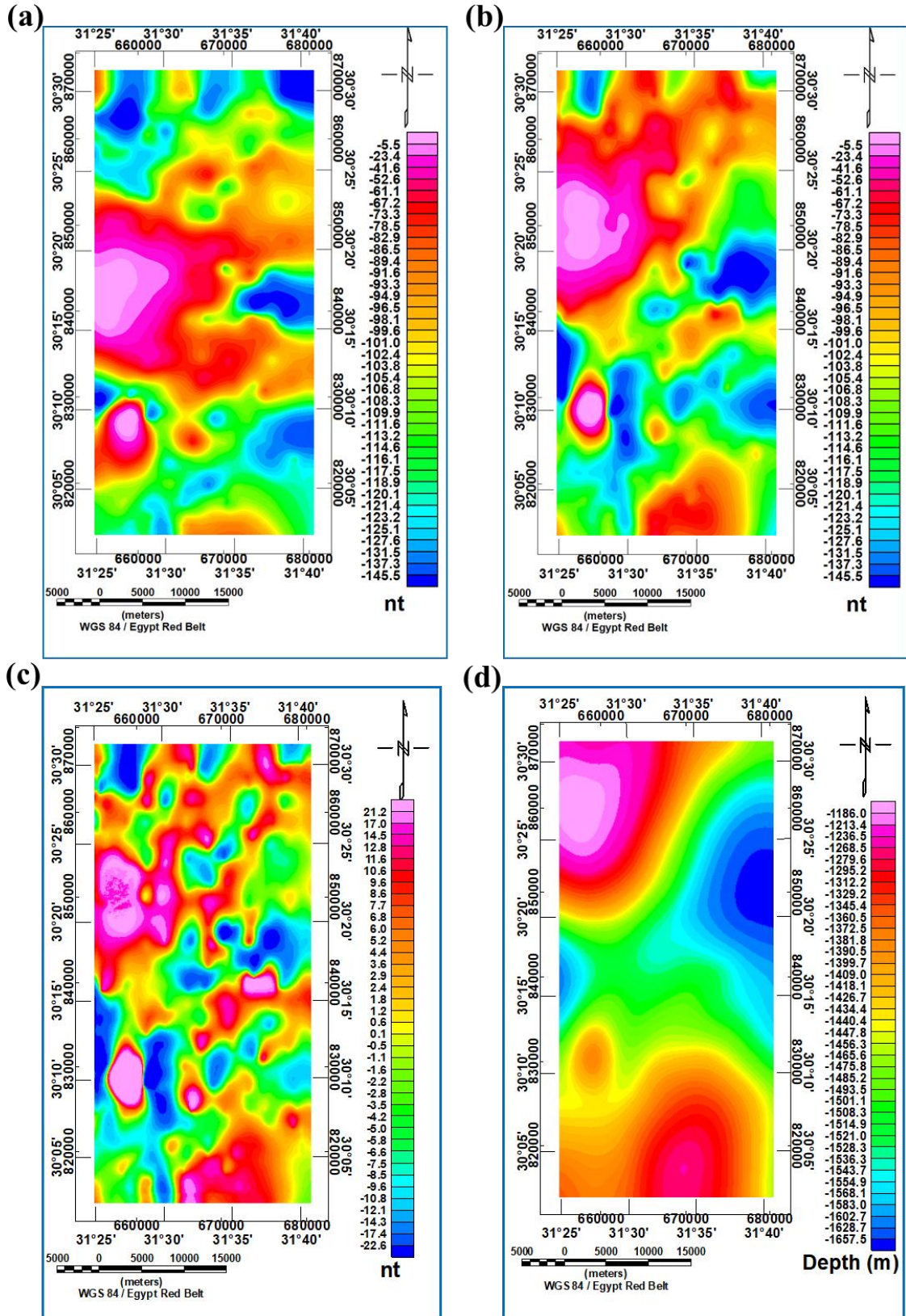


Fig. 15. (a) Observed; (b) Calculated magnetic anomaly; (c) Error percentage; and (d) Depth to basement surface magnetic model of area under investigation.

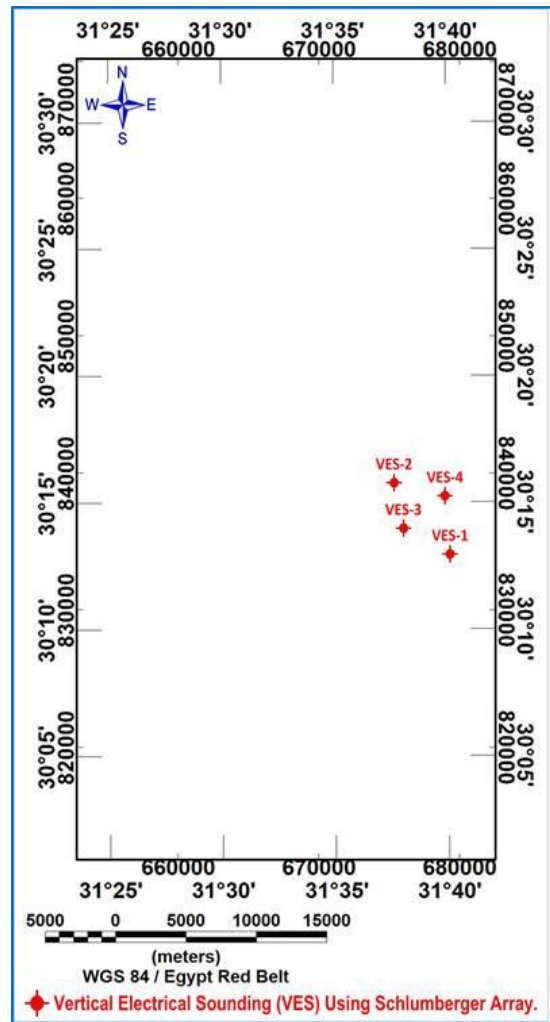


Fig. 16. Layout of four vertical electrical soundings.

The area seismicity

Despite of the low seismic activity in Egypt, the seismic risk can be considerable. The reason behind is that the recorded earthquakes mostly arise near to high-populated villages and cities, in addition to, the old construction methods. The different soil features in the different Egyptian locations and their effect on the seismic wave weakening are significant factors controlling earthquake risks (El Baz and Riad, 2002). Table 1 shows the earthquake actions happened in and around the investigation area. So, the construction practice has to be at least 500 m away from the fault locality.

Table 1 The earthquake happened in and around the investigation area.

Latitude	Longitude	Magnitude	day	Month	year
30.09	31.42	4.19	28	1	1900
30.1	31.5	4.4	6	3	1900
30.1	31.5	3.9	7	12	1900
30.1	31.6	5.7	29	3	1903
30.1	31.5	7	4	12	1905
30.1	31.5	5.5	26	12	1906
30.16	31.45	5	26	12	1906
30.17	31.57	4.7	10	6	1907
30.2	31.5	5	22	6	1907
30.2	31.5	5.2	22	7	1907
30.2	31.5	5	23	2	1909
30.2	31.58	5	10	7	1910
30.21	31.51	3.7	26	1	1911
30.21	31.51	7	4	4	1911
30.24	31.5	3.5	13	7	1911
30.24	31.62	4.2	22	8	1911
30.25	31.53	3.5	12	11	1911
30.27	31.5	3.5	15	11	1911
30.28	31.51	5.2	27	2	1913
30.29	31.42	6.2	16	9	1913
30.3	31.6	4	13	11	1913
30.3	31.5	7.1	3	10	1914
30.31	31.58	4.9	4	10	1914

30.31	31.44	5.5	21	5	1915
30.33	31.46	2	30	1	1916
30.34	31.62	2	9	1	1917
30.35	31.46	4	22	2	1917
30.35	31.66	6.5	29	9	1918
30.37	31.59	5.8	30	6	1919
30.4	31.5	5	30	6	1919
30.4	31.6	5	19	8	1919
30.4	31.6	2	11	6	1920
30.4	31.6	4.6	1	10	1920
30.4	31.6	4	21	4	1921
30.4	31.64	5	16	3	1922
30.41	31.58	5.5	2	4	1922
30.41	31.65	4.1	18	6	1922
30.43	31.63	3	24	6	1922
30.47	31.43	4	29	8	1922
30.47	31.56	4	7	9	1922
30.5	31.5	3	7	1	1923
30.5	31.6	4.3	27	2	1923
30.5	31.6	4.2	8	12	1923
30.5	31.5	6	18	2	1924
30.5	31.6	5	27	2	1924
30.5	31.6	4.8	9	6	1924
30.5	31.6	4.8	13	9	1924

30.5	31.6	5.2	27	1	1925
30.5	31.5	4	16	3	1925
30.5	31.5	4.2	9	5	1925
30.5	31.6	8	26	6	1926
30.5	31.6	2	9	7	1926
30.5	31.6	2	9	7	1926
30.5	31.5	2	19	8	1926
30.5	31.6	2.5	5	9	1926
30.5	31.6	4.6	2	5	1927
30.5	31.6	3	6	6	1927
30.5	31.5	6	11	7	1927
30.5	31.6	3.5	13	7	1927
30.5	31.6	4.5	17	7	1927
30.5	31.6	4.8	24	9	1927
30.5	31.6	3.5	18	10	1927
30.5	31.5	5.1	12	12	1927
30.5	31.6	4.2	18	1	1928
30.5	31.6	4	3	2	1928
30.5	31.6	2	4	2	1928

RESULTS AND DISCUSSION

The Bouguer map revealed that the gravitational field rises towards the north direction. The comparison between the RTP and the original TMI maps showed a northward shift in the original anomalies locations. This shift is due to the exclusion of the magnetic field declination and inclination angles. The Bouguer and RTP maps reveal several causative sources with varying amplitudes and frequencies.

The regional-residual separation technique was executed on the Bouguer and RTP maps for the separation of the deep anomalies from shallower ones. This filtration

technique was done within the frequency domain using power spectral analysis. The calculated depths of the residual and regional gravity sources were 0.48 km and 2.74 km, respectively. In contrast, the depths for residual and regional magnetic sources were 0.5 km and 2.33 km, respectively. It can be concluded that Euler solution using $SI=0$ is the best one where the clustering of solutions is more obvious for the magnetic and gravity data.

The fault trends in the Bouguer and RTP maps are the same in the low pass filtered maps and this indicates the faults tectonic nature that extended from shallow to high depths. The similarity of the fault trends in the Bouguer, RTP, and the high pass filtered maps reflects that these fault trends extend within the subsurface up to the shallow depths. In addition, the various orientations of the smaller anomalies reflect the different stress regimes of the new tectonics on the shallow subsurface.

The rose diagrams displayed the tectonics orientation deduced from the low, high filtered, and Euler solution maps. Through the inspection of the rose diagrams, it can be noticed that the most common tectonic trends prevailing in the deeper levels for the gravity and magnetic data are the NE-SW (45° - 60°) and E-W. On the other hand, the most common tectonic trends prevailing in the shallow levels are NE-SW and N-S (45° - 60°). The dominant tectonic trend from the Euler solution is $N45^{\circ}W$ prevailing in shallow-intermediate levels for the gravity data. In contrast, the magnetic showed that the dominant tectonic trend is N-S and NE-SW prevailing in shallow-intermediate levels.

The results of 3-D magnetic analysis reflected that the sedimentary cover thickness is about 1.186 km in the northwest and south and 1.657 Km within the central parts. The results of the low, high pass filtered and Euler solution maps reveal that dissection of the area by several faults. These fault trends coincided with the directions of the Gulf of Suez, Gulf of Aqaba, River Nile system, and Mediterranean tectonics.

(Fig. 17a) showed the measured resistivity data (black line) for four VES and calculated data (red line). The results of inverted models were showed by the thicknesses and true resistivities of the geo-electrical layers. The error percentage between the calculated and measured apparent resistivity curves was measured by root mean square error (RMS) value. The RMS values for the four VES ranged between 8.74% and 24.1%.

(Fig. 17b) revealed the lithology through the inverted true resistivity of four VES with the same datum at elevation 130 m. Also, it showed the water table depth to be 70 and 60m for only VES 1 and VES 4, respectively.

Finally, the faults are natural phenomena and it is important to detect their positions during urban planning. The results of this investigation provide the information about the position and extension of the existing faults in the study area. We recommend taking these faults positions in consideration, avoiding the building over them and customization of green spaces above them.

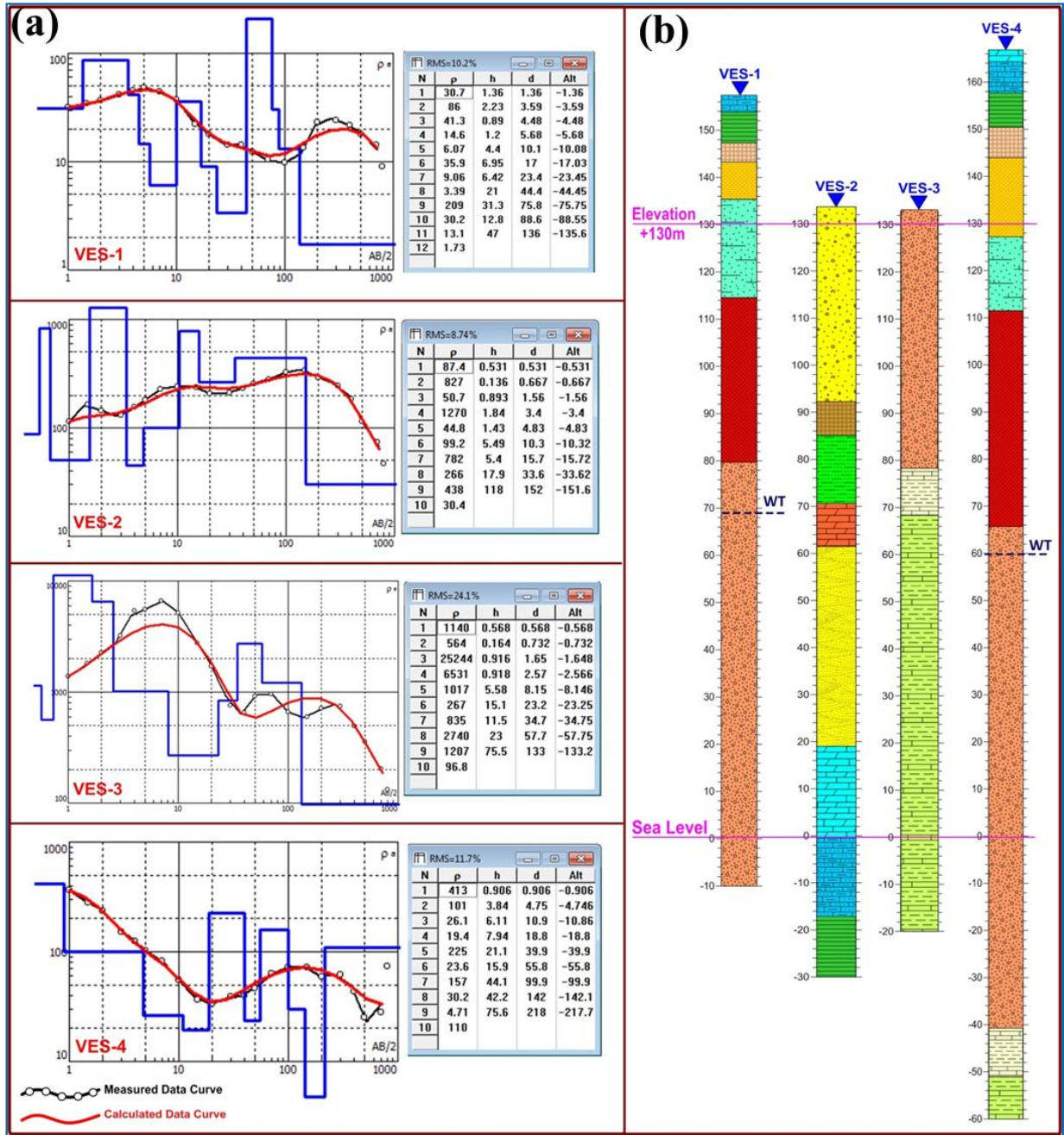


Fig. 16. (a) VES (1-4) apparent resistivity models and table shows true resistivities and thicknesses for the geo-electric layers calculated from the inverted apparent resistivity models; and (b) The inverted true resistivity of four VES with the same datum at elevation (130 m).

CONCLUSION

Through the gravity and magnetic study, we can conclude that: The dissection of the area by several faults of directions NE-SW matching the Gulf of Aqaba, NW-SE matching the Gulf of Suez, N-S matching the River Nile system, and E-W matching the Mediterranean tectonics. The basement depth is ranging from 1186 to 1683 m.

The geo-electrical method was used to explore groundwater; it presented the water table depth to be 70 and 60m for only VES 1 and VES 4, respectively. The positions that include faults are considered hazardous places for construction, it is recommended to avoid such places. The positions that don't include faults are safer and more suitable for constructing buildings; these positions are found in the south of the survey site.

REFERENCES

- Afolabi, O.; Amigun, J.O. and Ako, B.D.** (2012). Euler 3-D deconvolution of analytical signal of magnetic anomalies over iron ore deposit in Okene, Nigeria. *Journal of Emerging Trends in Engineering and Applied Sciences* 3(4): 711-717.
- Araffa, S.A.S.** (2013). Delineation of groundwater aquifer and subsurface structures on North Cairo, Egypt, using integrated interpretation of magnetic, gravity, geoelectrical and geochemical data. *Geophysical Journal International* 192 (1): 94-112.
- Araffa, S.A.S.; Santos, F.A.M. and Arafa-Hamed, T.** (2014). Assessment of subsurface structural elements around greater Cairo by using integrated geophysical tools. *Environmental earth sciences* 71(8): 3293-3305.
- Araffa, S.A.S.; Sabet, H.S. and Gaweish, W.R.** (2015). Integrated geophysical interpretation for delineating the structural elements and groundwater aquifers at central part of Sinai Peninsula, Egypt. *Journal of African Earth Sciences* 105: 93-106.
- Araffa, S.A.S.; Soliman, S.A.; Ghamry, E.; El Khafif, A.; Khashba, A. and Soliman, A.S.** (2017). Contribution of geophysical studies on detection of the Petrified Frost Qattamiya, Cairo, Egypt. *Egyptian Journal of Petroleum* 26(1): 145-156.
- Araffa, S.A.S.; Soliman, S.A.; El Khafif, A.; Younis, A. and Shazley, T.F.** (2019). Environmental investigation using geophysical data at East Sadat City, Egypt. *Egyptian Journal of Petroleum* 28(1): 117-125.
- El-Awady, M.M.; El-Badrawy, H.T.; El-Ela, A.M.A.; Solimaan, M.R.; Alrefae, H.A. and Elbowab, M.** (2016). Integrated geophysical studies on the area east of Abu Gharadig basin, southern Cairo, Egypt, using potential field data. *NRIAG Journal of Astronomy and Geophysics* 5(2): 351-361.
- El Baz, F. and Riad, S.** (2002). Seismic hazard and seismotectonic of Egypt, Cairo UNESCO Office.
- El Dawi, M.G.; Tianyou, L.; Hui, S. and Dapeng, L.** (2004). Depth estimation of 2-D magnetic anomalous sources by using Euler deconvolution method. *American Journal of Applied Sciences* 1(3): 209-214.
- El-Fayoumy, I. F.** (1968). Geology of groundwater supplies in the region east of the Nile Delta. Unpublished Ph. D. Thesis, Fac. of Sci., Geology Department, Cairo Univ., Egypt.
- Foulger, G. and Pierce, C.** (2007). *Geophysical Methods in Geology. Teaching Handbook*, University of Durham, UK, 78 pp.

- Garcia, J.G. and Ness, G.E.** (1994). Inversion of the power spectrum from magnetic anomalies. *Geophysics* 59(3): 391-401.
- Geng, M.; Ali, M.Y.; Fairhead, J.D.; Bouzidi, Y. and Barkat, B.** (2020). Morphology of the basement and Hormuz salt distribution in offshore Abu Dhabi from constrained 3-D inversion of gravity and magnetic data. *Tectonophysics* 791, 228563.
- Hashem, W.** (1997). Engineering geology of El Obou'r'City East of Cairo, Egypt. M. Sc. Thesis, Fac. of Sci., Geology Department, Ain Shams Univ., Egypt.
- Khalil, A.; Abdel Hafeez, T.H.; Saleh, H.S. and Mohamed, W.H.** (2016). Inferring the subsurface basement depth and the structural trends as deduced from aeromagnetic data at West BeniSuef area, Western Desert, Egypt. *NRIAG Journal of Astronomy and Geophysics* 5(2): 380-392.
- Luo, Y.; XUE, D. J. and WANG, M.** (2010). Reduction to the Pole at the Geomagnetic Equator. *Chinese Journal of Geophysics* 53(6): 1082-1089.
- Maurizio, F.; Tatina, Q. and Angelo, S.** (1998). Exploration of a lignite bearing in Northern Ireland, using ground magnetic. *Geophysics* 62(4): 1143-1150.
- Mickus, K.** (1980). Gravity Method. *Geophysics* 45(11).
- Mohamed, S. and El-Sabrouty, M. N.** (2014). Applications of hydrogeochemical modeling to assessment geochemical evolution of the Quaternary aquifer system in Belbies area, East Nile Delta, Egypt. *Journal of Biology and Earth Sciences* 4(1): E34-E47.
- Mohamed, A.M.E.; El-Hussain, I.; Deif, A.; Araffa, S.A.S.; Mansour, K. and Al-Rawas, G.** (2019). Integrated ground penetrating radar, electrical resistivity tomography and multichannel analysis of surface waves for detecting near-surface caverns at Duqm area, Sultanate of Oman. *Near Surface Geophysics* 17(4): 379-401.
- Reid, A.B.; Alsop, J.M.; Grandier, H.; Mille, A.J. and Somerton, I.W.** (1990). Magnetic interpretation in three dimensions using Euler deconvolution. *Geophysics* 55: 80-91.
- Spector, A. and Grant, F.S.** (1970). Statistical models for interpreting aeromagnetic data. *Geophysics* 35(2): 293-302.
- Sultan, S.A.; Santos, F.A. and Helaly, A.S.** (2011). Integrated geophysical interpretation for the area located at the eastern part of Ismailia Canal, Greater Cairo, Egypt. *Arabian Journal of Geosciences* 4(5-6): 735-753.
- Thompson, D.T.** (1982). EULDPH: A new technique for making computer-assisted depth estimates from magnetic data. *Geophysics* 47(1): 31-37.